A Variable Temperature Neutron Diffraction Study of the Oxide Ion Conductor Ba$_3$VWO$_{8.5}$

Asma Gilane [a, b], Sacha Fop [a, c], Dylan N. Tawse [a], Clemens Ritter [d] and Abbie C. Mclaughlin [a*]

a The Chemistry Department, University of Aberdeen, Meston Walk, Aberdeen AB24 3UE, United Kingdom

b Department of Chemistry and Chemical Engineering, SBA School of Science and Engineering, Lahore University of Management Sciences (LUMS), Lahore, Pakistan.

c ISIS Facility, Rutherford Appleton Laboratory, Harwell Campus, Didcot, OX11 0QX, United Kingdom.

d Institut Laue Langevin, 71 Avenue des Martyrs, BP 156, F-38042 Grenoble Cedex 9, France.

* a.c.mclaughlin@abdn.ac.uk

Abstract

Ba$_3$VWO$_{8.5}$ is an oxide ion conductor with a bulk conductivity of 5.0×10^{-5} S cm^{-1} at 600 °C. Ba$_3$VWO$_{8.5}$ is anomalous to the other Ba$_3$M'M''O$_{8.5}$ (M' = Nb; M'' = Mo, W) oxide ionic conductors, as it exhibits cation order with vanadium and tungsten on the M1 site only. Here we report a variable temperature neutron diffraction study of Ba$_3$VWO$_{8.5}$ that demonstrates cation order is retained up to 800 °C. We show for the first time that the structural rearrangements reported for hexagonal perovskite derivatives Ba$_3$M'M''O$_{8.5}$ are dictated by water absorption. The significant water uptake in Ba$_3$M'M''O$_{8.5}$ (M' = Nb; M'' = Mo, W) arises due to the flexibility of the crystal structure, whereby upon absorption of water, a fraction of the transition metal cations moves from the M1 site to the octahedral M2 site. The results presented here demonstrate that the presence of 50% V^{5+} on the M1 site, which has a strong preference for tetrahedral geometry, is enough to disrupt the flexibility of the cation sublattice resulting in the ordering of the cations exclusively on the M1 site and no significant water absorption.

Introduction

Oxide ion conductors have recently drawn great attention due to their application as electrolytes in energy conversion technologies such as solid oxide fuel cells (SOFCs) and solid oxide electrolysis cells and devices i.e. oxygen separation membranes and oxygen sensors.[1,2] Specifically, SOFCs provide clean energy from sustainable sources, high energy conversion efficiency[3] and fuel flexibility with negligible emissions of pollutants.[4,5] The major drawback associated with SOFCs is the high operating temperature (800-1000 $^\circ$C) required for ionic transport in commercially available electrolyte materials which leads to high cost, poor durability, component degradation, and technical challenges in materials compatibility, limiting the wide range of applications of SOFCs [1,2]. The oxide ionic conductivity of a material is highly dependent on its crystal structure and it is mediated by oxygen vacancies and interstitial atoms. Therefore, new structural families are sought as alternative electrolyte materials that exhibit high conductivity of oxide ions at intermediate temperatures (300-600 °C).

Oxide ion conductivity has been reported in various materials with different crystal structures including fluorite-related systems,[6-7] lanthanum silicate and germanium apatites,[8-9] $La_2Mo_2O_9$ (LAMOX)-based materials,[10] $Bi_4V_2O_{11}$ (BIMEVOX)-based derivatives,[11] perovskite oxides [12-13] and perovskite derivatives.[14] Recently, significant oxide ion conductivity has been reported in the hexagonal cation-deficient perovskite derivative $Ba_3M'M''O_{8.5}$ (M' = Nb, V; M'' = Mo, W).[15-19] Recent results have shown that by substitution of Nb^{5+} by V^{5+} to form $Ba_3Nb_{0.9}V_{0.1}MoO_{8.5}$, it is possible to enhance the bulk conductivity to 0.01 Scm^{-1} at 600 °C, [19] that is one order of magnitude greater than observed for $Ba_3NbMoO_{8.5}$.[16] The $Ba_3M'M''O_{8.5}$ phases exhibit a unique crystal structure which is composed of a hybrid of the 9R hexagonal perovskite ($A_3B_3O_9$) and palmierite ($A_3B_2O_8$) units. The 9R hexagonal perovskite polytype is described by the stacking along the c axis of nine BaO_3 layers with the stacking sequence (hhc)$_3$ and trimers of face sharing MO_6 octahedra connected via corner sharing. The replacement of the cubic AO_3 layer with an oxygen deficient AO_2 layer results in the palmierite structure which consists of isolated MO_4 tetrahedra. In $Ba_3M'M''O_{8.5}$ there is partial occupation of two crystallographic oxygen positions (O2 and O3) within the palmierite-like (P-L) layer (Figure 1) resulting in variable coordination $M1O_x$ polyhedral units.[16,20] The cation vacancies are disordered on two mutually exclusive metal positions (M1 and M2), thus resulting in hybrid trimer stacks of face sharing polyhedral units. [19, 21] The oxide ion and cation disorder observed within the structure leads to the high oxide ionic conductivity.

We have recently reported oxide ion conductivity in the hexagonal perovskite derivative $Ba_3VWO_{8.5}$.[22] $Ba_3VWO_{8.5}$ also exhibits the hybrid structural model like the other $Ba_3M'M''O_{8.5}$ hexagonal perovskite derivatives, but significant differences exist in the average structure of $Ba_3VWO_{8.5}$. A combined neutron and X-ray diffraction study revealed that the M1 site is fully occupied while the M2 site is empty in the average structure of $Ba_3VWO_{8.5}$. Consequently, the $M1O_x$ polyhedral units are separated by empty octahedral cavities and the cationic vacancies are found exclusively on the M2 site.[22] Analysis of bond-valence site energy (BVSE) calculations on the different conduction pathways shows that the ordered cationic vacancies on M2 sites hinders the long range oxygen diffusion along c, restricting the conduction mechanism to a 2-dimensional pathway, which results in a significant reduction of the bulk conductivity of this compound (5.0×10^{-5} S cm^{-1} at 600 °C). Here, we perform a variable temperature neutron diffraction study of $Ba_3VWO_{8.5}$ from 30 °C to 800 °C to further explore the correlation of structural and transport properties.

Experimental

$Ba_3VWO_{8.5}$ was synthesized via solid state reaction of stoichiometric amounts of $Ba(NO_3)_2$ (99.999%, Aldrich), V_2O_5 ($\geq$ 99.6%, Aldrich), and WO_3 (99.9%, Aldrich) as described previously.[22] X-ray powder diffraction data were collected at room temperature using a PANalytical Empyrean diffractometer equipped with a Cu Kα tube and a Johansson monochromator. Data were collected in the range 5 ° < 2θ < 120 ° with a step size of 0.013°. Variable temperature neutron diffraction data were collected by heating the sample in air at selected temperatures between 30 °C – 800 °C on the high-resolution diffractometer D2B at the Institut Laue Langevin (ILL) in Grenoble. A 5 g sample of $Ba_3VWO_{8.5}$ was loaded into an open quartz tube (to prevent reduction of W under vacuum) and data were recorded for two hours at each temperature.[23] The empty quartz tube was also measured at selected temperatures and this data was used to subtract its contribution to the background. Rietveld refinements were performed using the GSAS/EXPGUI package.[24,25] The background was fitted by the Chebyschev polynomial function while peak profiles were fitted with a pseudo-Voigt function.

Maximum entropy (MEM) analysis was performed with the software Dysnomia, [26] employing the structure factors obtained by Rietveld refinement of the neutron diffraction data. MEM is a model-free method based on the calculation of scattering density from a limited amount of information (unit cell, symmetry, structure factors) by maximizing the information entropy under restraints, consistent with experimental observation. Neutron scattering density distributions at various temperatures were reconstructed by MEM calculations with the unit cell divided into 84 x 84 x 236 pixels.

Thermogravimetric analysis (TGA) was performed with a Mettler Toledo TGA 2 coupled with a Hiden Quadrupole Mass Spectrometer (MS) in static air, with a heating rate of 10 °C/min. Measurements were performed on a sample stored under ambient conditions, and after a two-hour preheat to remove adsorbed species as described in the supplementary information.

Results and Discussion

The X-ray diffraction pattern demonstrates that $Ba_3VWO_{8.5}$ is phase pure and can be indexed with the $R\bar{3}m$ H space group as previously reported.[22] The crystal structure of $Ba_3VWO_{8.5}$ is displayed in Figure 1 showing the V/W cation vacancies on the M2 ($3b$) site. The O1 site is fully occupied but there is partial occupation of the average O2 and O3 crystallographic sites and positional disorder of both O2 and O3 is observed resulting in 4-, 5, and 6-fold coordination geometries on the local scale. As common to the $Ba_3M'M''O_{8.5}$ family, O3 is modelled by position $36i$ rather than the $6c$ position normally observed for the palmierite structure because of the positional disorder of the oxygen atom.[16-21] The Ba atoms fractional occupancies refined to within ±1% of full occupancy and were fixed at 1.0.
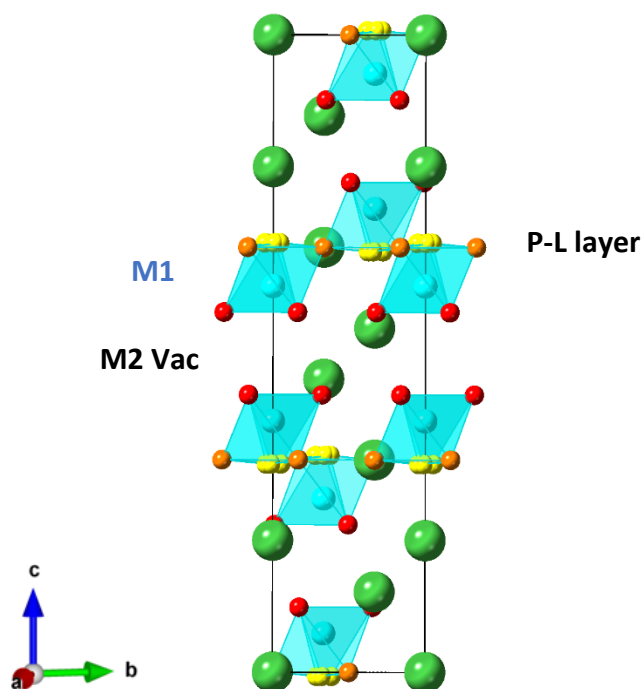

Figure 1 The crystal structure of $Ba_3VWO_{8.5}$. The M1 site ($6c$, within the blue polyhedra) is occupied by V/W whilst cation vacancies are ordered on the M2 site. The green spheres represent the Ba atoms, while the oxygen atoms are represented by red (O1), orange (O2) and yellow (O3) spheres.

An excellent fit to this model was obtained from the neutron diffraction data at both 30 °C and 800 °C as shown in Figure 2 with statistical parameters χ^2 =2.36, R_p = 4.79%, R_{wp} = 5.76%, R_F^2 = 2.90% at 30 °C (Table S1). The Rietveld fits to the $R\bar{3}m\ H$ crystallographic model of $Ba_3VWO_{8.5}$ at further selected temperatures between 30 °C and 800 °C are shown in Figure S1. A very good fit is obtained at all temperatures so that there is no change in crystallographic symmetry up to 800 °C.
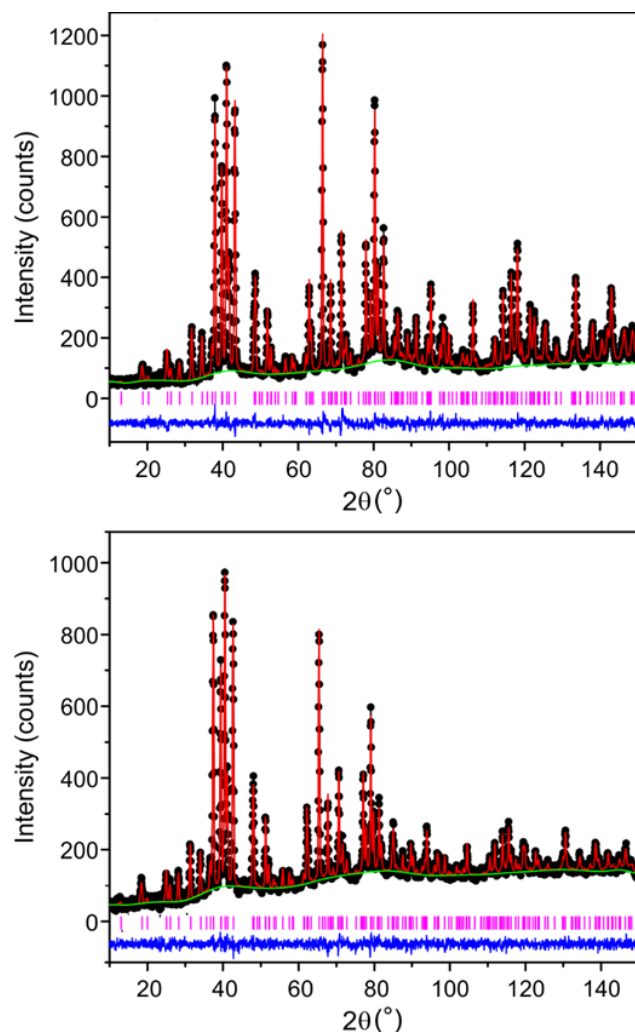

Figure 2 Rietveld fits to the $R\bar{3}m\ H$ crystallographic model of $Ba_3VWO_{8.5}$ at 30 °C (top) and 800 °C (bottom) from neutron diffraction data. The black dots are the observed data and the red line is the Rietveld fit. The difference between the observed and the calculated patterns is shown by the blue line, the pink vertical bars indicate the reflection positions and the green line is the background function.

The maximum entropy method (MEM) was employed to visualize the oxide ion conduction pathway within the $Ba_3VWO_{8.5}$ crystal structure. MEM analysis of variable temperature neutron diffraction data is a well-established method for the experimental visualization of diffusion pathways in ionic conductors.

5

[27-29] The neutron scattering density was reconstructed by using the structure factors obtained by Rietveld analysis of the variable temperature neutron diffraction data. Figure 3a shows the obtained scattering densities at 30 °C and 800 °C.
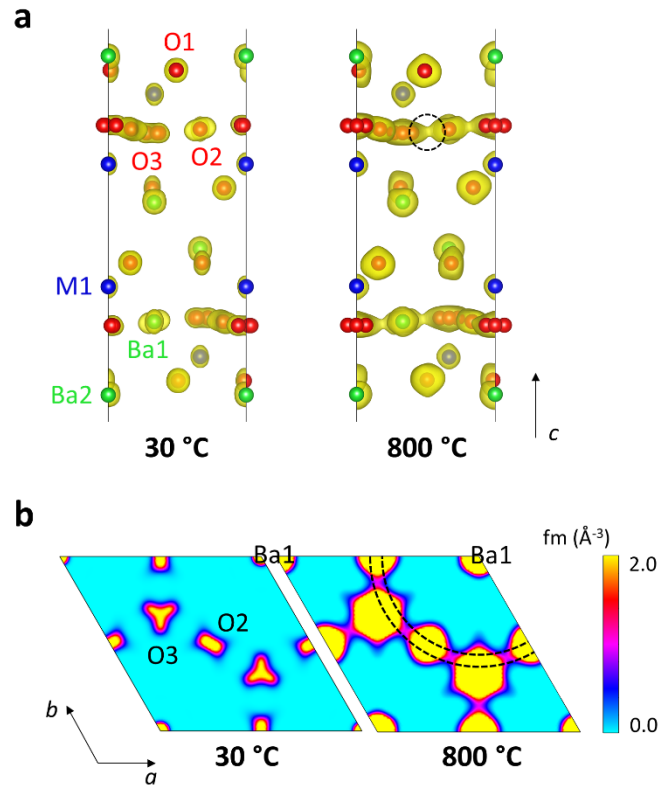

Figure 3 a) Nuclear scattering density isosurfaces at 30 °C and 800 °C obtained by MEM analysis as seen along the [100] direction. The dashed circle highlights the connected distribution of oxide ions within the P-L layer at 800 °C. **b)** Maximum entropy maps showing the nuclear scattering density distribution along the P-L layer, at $z = 0$ as seen along the [001] direction. The dashed lines represent a curved migration trajectory.

The results from MEM analysis, [27-29] evidences no scattering density at the M2 site, thus confirming that the cation vacancies are entirely on the M2 site in the $Ba_3VWO_{8.5}$ structure at all temperatures. Connecting distributions of oxide ions are visible along the P-L layer at 800 °C (highlighted by a dashed circle in figure 3a), evidencing a 2-dimensional oxide ion conduction pathway along the partially occupied O2 and O3 crystallographic sites. The view along the perpendicular [001] direction demonstrates a curved O2–O3 migration trajectory around the Ba1 cation (Figure 3b). Oxide ion diffusion occurs via a tetrahedral-octahedral interchange (interstitialcy) mechanism, over the O2-O2-O2

face of the M1O$_6$ pseudo-octahedron, in agreement with the conduction mechanism reported for Ba$_3$NbMoO$_{8.5}$. [30]
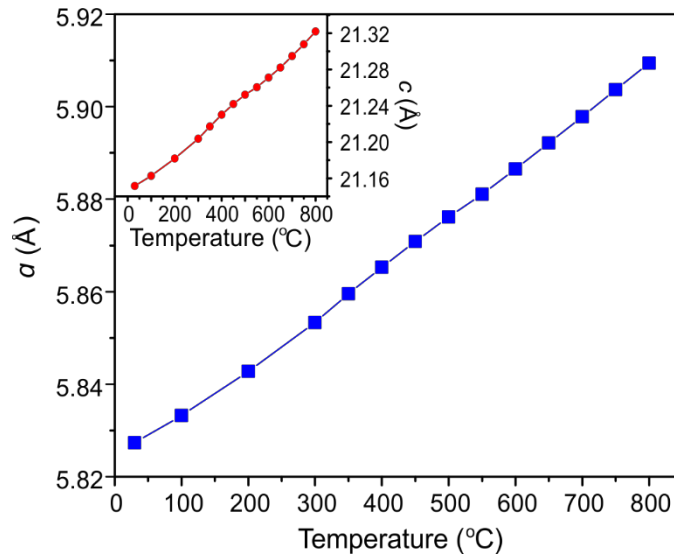

Figure 4 The variation of the *a* cell parameter with temperature. The inset shows the thermal dependence of the *c* cell parameter.

Figure 4 displays the thermal variation of the cell parameters and there is no evidence of any significant deviation from linear thermal expansion. The M-O2 and M-O3 bond lengths are shown in Figure S2; where an increase in both bond lengths is observed upon heating from 30 °C to 800 °C. Figure 5 shows the variation of the fractional occupancies of the average octahedral O2 and tetrahedral O3 positions which demonstrates that upon increasing the temperature from 30 °C to 800 °C there is a very small, but regular increase in the number of tetrahedral units in the P-L layer and a concomitant decrease in the number of octahedral units. This is in stark contrast to both Ba$_3$NbMoO$_{8.5}$ and Ba$_3$W$_{1.2}$Nb$_{0.8}$O$_{8.6}$ where variable temperature neutron diffraction studies have revealed that a significant structural rearrangement occurs above 300 °C due to the change in the relative occupancy of O2 and O3 sites.[31, 32] The redistribution of oxygen sites over O2 and O3 leads to a sizeable increase in the ratio of (M'/M'')O$_4$ tetrahedra to (M'/M'')O$_6$ octahedra in the average structure and as a result, the ionic conductivity is enhanced. At the same time there is a redistribution of the M'/M'' cations from the M2 to the M1 site.[31,32] In Ba$_3$NbMoO$_{8.5}$ and Ba$_3$W$_{1.2}$Nb$_{0.8}$O$_{8.6}$ the percentage of tetrahedral units in the P-L layer change significantly from 50% and 13% at 25 °C to 64.5% and 45.5% respectively at 600 °C and there is a clear relationship between the structural rearrangement and the activation energy for oxide ion conduction. [31, 32] On the contrary, in Ba$_3$VWO$_{8.5}$ there is very little change in the geometry of the P-L layer. At 30 °C

the percentage of tetrahedral units within the P-L layer is 65.3% which increases to 67.6% at 800 °C and there is no change in the activation energy for oxide ion conduction upon heating. [22]
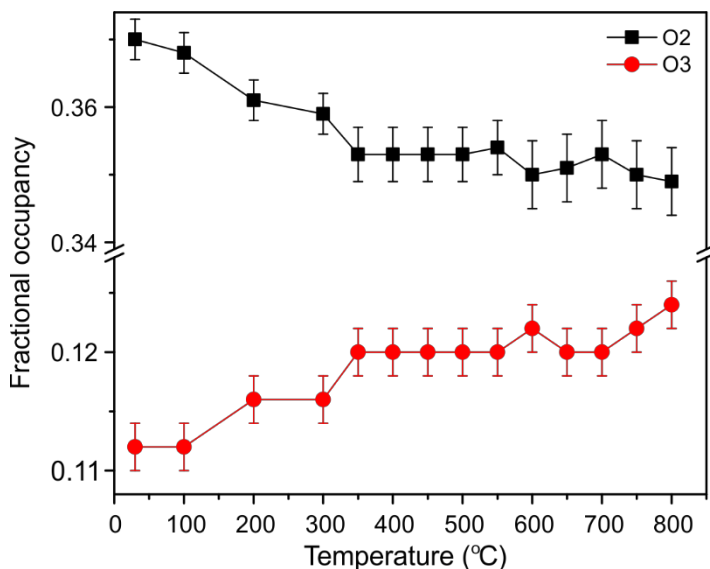

Figure 5. The temperature variation of the fractional occupancies of the octahedral O2 and tetrahedral O3 showing a small and regular increase in the number of tetrahedral units in the P-L layer and a concomitant decrease in the number of octahedral units.

At 30 °C $Ba_3VWO_{8.5}$ exhibits a much higher proportion of tetrahedral units in the P-L layer (~65.3%) than $Ba_3NbMoO_{8.5}$ (~50%). This ratio is dependent on the geometrical preference of the cations. Both V^{5+} and Mo^{6+} prefer tetrahedral geometry while Nb^{5+} and W^{6+} typically adopt octahedral geometry.[33] In corroboration, $Ba_{2.69}VMoO_{8.20}$ contains 86.8% tetrahedra within the average structure at room temperature.[34] The redistribution of the *M'/M''* cations from the M2 to the M1 site in $Ba_3NbMoO_{8.5}$ and $Ba_3W_{1.2}Nb_{0.8}O_{8.6}$ facilitates the structural rearrangement of the O2 and O3 fractional occupancies above 300 °C. This is not possible in $Ba_3VWO_{8.5}$ as the M2 site is vacant and hence very little change in the geometry of the P-L layer is observed upon heating. We have recently shown that the occupancy of M2 and subsequent cation disorder in the hexagonal perovskite derivatives $Ba_3NbMoO_{8.5}$ and $Ba_7Nb_4MoO_{20}$ arises due to water absorption.[35, 36] Both phases uptake a significant amount of water [35] in the P-L layer and density functional theory geometry optimization calculations show that if a proton occupies a position between an O2/O3 site and M1, it forces movement of M1 to the M2 site.[36] The results from the calculations are supported by in situ neutron diffraction studies and maximum entropy (MEM) analysis of the neutron diffraction data.[36] In order to further investigate why the M2 site is vacant in $Ba_3VWO_{8.5}$ we have recorded thermogravimetric analysis data coupled to a mass spectrometer (TGA-MS) between

25 °C and 1000 °C. The results from TGA-MS are shown in Figures S3-5 and demonstrate a mass loss of 0.28%. The results show that there is no significant water loss over this temperature range and that the mass loss is due to very small amounts of CO_2 and O_2 (Figure S5). There was no evidence of oxygen loss from the neutron diffraction study. These results are in stark contrast to $Ba_3NbMoO_{8.5}$ and $Ba_7Nb_4MoO_{20}$ which absorb ~ 0.2 and 0.8 molecules of H_2O per formula unit respectively. [35, 36] The sizeable water absorption in both compounds arises due to the flexibility of the cation sublattice and is enabled by the movement of Nb/Mo from the M1 to the M2 site. The results presented here demonstrates that the presence of 50% V^{5+} on the M1 site, which has a strong preference for tetrahedral geometry, [33] is enough to disrupt the flexibility of the cation sublattice resulting in cation order on the M1 site and no significant water absorption. The loss of cation disorder further results in no long-range oxygen diffusion along c so that $Ba_3VWO_{8.5}$ has the lowest oxide ionic conductivity of all $Ba_3M'M''O_{8.5}$ phases. [22] These results also highly suggest that it is the presence of water within the structure that leads to the structural rearrangement observed above 300 °C in $Ba_3W_{1.2}Nb_{0.8}O_{8.6}$, $Ba_3NbMoO_{8.5}$ and $Ba_7Nb_4MoO_{20}$. As water leaves the structure, the M2 cations return to the M1 site with subsequent rearrangement of the oxygen population. [31, 32, 35, 36]

To investigate this further, the polyhedral distortion was evaluated by using the PIEFACE software. [37] Figure 6(a) shows the thermal variation of the polyhedral distortion for $Ba_3VWO_{8.5}$ compared to $Ba_3NbMoO_{8.5}$. The distortion of the $M1O_x$ units in $Ba_3VWO_{8.5}$ increases linearly with the temperature, while there is a clear non-linear behaviour for $Ba_3NbMO_{8.5}$, with a steep change in slope above 300 °C corresponding to the temperature at which this system exhibits a pronounced water loss. [35] These results show that the distortion of the $M1O_x$ units correlates with the concentration of water absorbed within the P-L layers. This is further corroborated by the thermal behaviour of the distortion of the polyhedral units along the P-L layer in $Ba_7Nb_4MoO_{20}$, which was calculated from in situ neutron diffraction data measured by cooling the sample under dry and humidified air atmospheres. [36] Under dry air, $\sigma(R)$ presents a linear behavior similar to $Ba_3VWO_{8.5}$. However, when water is absorbed by cooling the system in humidified air, there is a clear non-linear trend which once again corresponds with the characteristics of water uptake. [36] Similar trends can be seen in the displacement percentage of the M1 metal centers, which is calculated relative to the "equilibrium" position at the highest temperature, when the system is assumed to present the lowest level of hydration (Figure 6(b)). These results clearly demonstrate that it is the loss of water from the P-L layers upon heating which is the main driver in inducing the structural rearrangements and subsequent change in distortion of the $M1O_x$ units observed for $Ba_3NbM''O_{8.5}$ ($M'' = Mo^{6+}$, W^{6+}) and $Ba_7Nb_4MoO_{20}$. In both compounds the large amount of water absorbed results in migration of a fraction

9

of cations from the M1 site to the M2 site. Upon heating above 300 °C the water is lost from the P-L layer with simultaneous movement of the cations from the M2 site back to the M1 site. In $Ba_3VWO_{8.5}$ water absorption is inhibited by the presence of 50% V^{5+} at the M1 site which has a clear preference for tetrahedral geometry. As a result there are no cations at the M2 site and the structural rearrangement reported for $Ba_3NbM''O_{8.5}$ and $Ba_7Nb_4MoO_{20}$ is absent.
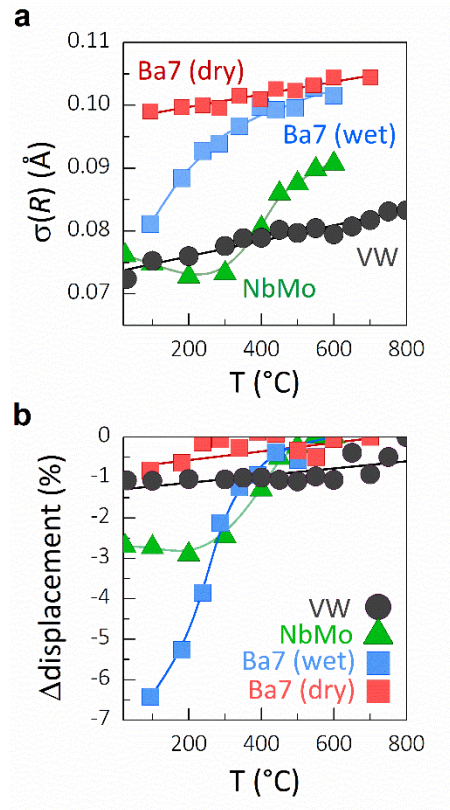

Figure 6. Thermal variation of the (a) the polyhedral distortion of the $M1O_x$ units along the P-L layers as quantified the standard deviation, $\sigma(R)$, of the three principal ellipsoid's radii via ellipsoidal analysis. (b) The displacement percentage of the M1 metal centres, which is calculated relative to the "equilibrium" position at the highest temperature. Results for $Ba_3VWO_{8.5}$ (VW) are compared with $Ba_3NbMO_{8.5}$ (NbMo) [15] and $Ba_7Nb_4MoO_{20}$ (Ba7) employing the in-situ neutron diffraction data collected under humidified and dry air atmospheres. [36]

Conclusions

In summary the variable temperature neutron diffraction experiment on the oxide ion conductor $Ba_3VWO_{8.5}$ has yielded further important insight into the structure property relationships of the hexagonal perovskite derivative oxide ion conductors. The results show that the unusual structural rearrangement observed above ~ 300 °C in $Ba_3M'M''O_{8.5}$ ($M' = Nb$; $M'' = Mo, W$) arises due to loss of

absorbed water and that to obtain the highest ionic conductivities in hexagonal perovskite derivatives both cation disorder and 3D conductivity are necessary. Further exploration of hexagonal perovskite derivatives containing *M* cations that can support variable co-ordination numbers and geometries is warranted.

Associated Content

Supporting information consists of table of crystallographic data and figures showing Rietveld refinement fits and TG-MS data.

References

1.   A. J. Jacobson, Materials for solid oxide fuel cells. *Chem. Mater.*, 2009, **22**, 660-674.

2.   E. D. Wachsman and K. T. Lee, Lowering the temperature of solid oxide fuel cells. Science, 2011, 334, 935.

3.   S. J. Skinner and J. A. Kilner, Oxygen ion conductors. *Materials Today*, 2003**, 6**, 30-37.

4.   L. Malavasi, C. A. J. Fisher and M. S Islam, Oxide-ion and proton conducting electrolyte materials for clean energy applications: structural and mechanistic features. *Chemical Soc. Rev.*, 2010**, 39**, 4370-4387.

5.   J. W. Fergus, Electrolytes for solid oxide fuel cells. *Journal of Power Sources*, 2006, **162**, 30-40.

6.   C. R. A. Catlow, Transport in doped fluorite oxides. *Solid State Ionics*, 1984**, 12**, 67-73.

7.   X. Kuang, J. L. Payne, M. R. Johnson and I. Radosavljevic Evans, Remarkably high oxide ion conductivity at low temperature in an ordered fluorite-type superstructure. *Angewandte Chemie International Edition*, 2012, **51**, 690-694.

8.   E. Kendrick, M. S. Islam and P. R. Slater, Developing apatites for solid oxide fuel cells: insight into structural, transport and doping properties. *J. Mater. Chem.*, 2007, **17**, 3104-3111.

9.   E. Béchade, O. Masson, T. Iwata, I. Julien, K. Fukuda, P. Thomas and E. Champion, Diffusion path and conduction mechanism of oxide ions in apatite-type lanthanum silicates. *Chem. Mater.*, 2009, **21**, 2508-2517.

10.   P. Lacorre, F. Goutenoire, O. Bohnke, R. Retoux and Y. Laligant, Designing fast oxide-ion conductors based on $La_2Mo_2O_9$. *Nature*, 2000, **404**, 856-858.

11.   F. Abraham, M. F. Debreuille-Gresse, G. Mairesse and G. Nowogrocki, Phase transitions and ionic conductivity in $Bi_4V_2O_{11}$ an oxide with a layered structure. *Solid State Ionics*, 1988, **28**, 529-532.

12.   T. Ishihara, H. Matsuda and Y Takita, Doped $LaGaO_3$ perovskite type oxide as a new oxide ionic conductor. *J. Am. Chem. Soc.*, 1994, **116**, 3801-3803.

13.   M. Li, M. J. Pietrowski, R. A. De Souza, H. Zhang, I. M. Reaney, S. N. Cook, J. A. Kilner and D. C. Sinclair, A family of oxide ion conductors based on the ferroelectric perovskite $Na_{0.5}Bi_{0.5}TiO_3$. *Nat. Mater.*, 2014, **13**, 31-35.

14.   K. Fujii, Y. Esaki, K. Omoto, M. Yashima, A. Hoshikawa, T. Ishigaki and J. R. Hester, New perovskite-related structure family of oxide-ion conducting materials $NdBaInO_4$. *Chem. Mater.*, 2014, **26**, 2488-2491.

15.   S. Fop, K. S. McCombie, E. J. Wildman, J. M. S. Skakle and A. C. Mclaughlin, Hexagonal perovskite derivatives: a new direction in the design of oxide ion conducting materials. *Chem. Commun.*, 2019, **55**, 2127-2137.

16.   S. Fop, J. M. S. Skakle, A. C. McLaughlin, P. A. Connor, J. T. S. Irvine, R. I. Smith and E. J. Wildman, Oxide ion conductivity in the hexagonal perovskite derivative $Ba_3MoNbO_{8.5}$. *J. Am. Chem. Soc.*, 2016, **138**, 16764-16769.

17.   K. S. McCombie, E. J. Wildman, S. Fop, R. I Smith, J. M. S. Skakle and A. C. Mclaughlin, The crystal structure and electrical properties of the oxide ion conductor $Ba_3WNbO_{8.5}$. *J. Mater. Chem. A*, 2018, **6**, 5290-5295.

18.   A. Bernasconi, C. Tealdi and L. Malavasi, High-Temperature Structural Evolution in the $Ba_3Mo_{(1-x)}W_xNbO_{8.5}$ System and Correlation with Ionic Transport Properties. *Inorg. Chem.*, 2018, **57**, 6746-6752.

19.   S. Fop, K. S. McCombie, R. I. Smith and A. C. Mclaughlin, Enhanced Oxygen Ion Conductivity and Mechanistic Understanding in $Ba_3Nb_{1-x}V_xMoO_{8.5}$. *Chem. Mater.*, 2020, **32**, 4724-4733.

20.   M. S. Chambers, K. S. McCombie, J. E. Auckett, A. C. Mclaughlin, J. T. S. Irvine, P. A. Chater, J. S. O. Evans and I. R. Evans, Hexagonal perovskite related oxide ion conductor $Ba_3NbMoO_{8.5}$: phase

transition, temperature evolution of the local structure and properties. *J. Mater. Chem. A*, 2019, **7**, 25503-25510.

21.   J. E. Auckett, K. L. Milton and I. R. Evans, Cation Distributions and Anion Disorder in $Ba_3NbMO_{8.5}$ (M = Mo, W) Materials: Implications for Oxide Ion Conductivity. *Chem. Mater.*, 2019, **31**, 1715-1719.

22.   A. Gilane, S. Fop, F. Sher, R. I. Smith and A. C. Mclaughlin, The relationship between oxide-ion conductivity and cation vacancy order in the hybrid hexagonal perovskite $Ba_3VWO_{8.5}$. *J. Mater. Chem. A*, 2020, **8**, 16506-16514.

23.   A. Mclaughlin, S. Fop, C. Ritter and E. Wildman, High temperature structural study of the oxide ion conductor $Ba_3VWO_{8.5}$. Institut Laue-Langevin (ILL), 2020, doi:10.5291/ILL-DATA.5-23-737.

24.   R. B. Von Dreele and A. C. Larson, General structure analysis system (GSAS); Report LAUR 86−748; Los Alamos National Laboratory, 1994.

25.   B. H. Toby, EXPGUI, a graphical user interface for GSAS. *J. Appl. Crystallogr.*, 2001, **34**, 210–213.

26.   K. Momma, T. Ikeda, A. A. Belik and F. Izumi, Dysnomia, a computer Program for maximum-entropy method (MEM) analysis and its performance in the MEM-based pattern fitting. *Powder Diffraction*, 2013, **28**, 184-193.

27.   M. Yashima,Crystal structures, structural disorders and diffusion paths of ionic conductors from diffraction experiments. *Solid State Ionics*, 2008, **179**, 797-803.

28.   M. Yashima *et al*. Structural disorder and diffusional pathway of oxide ions in a doped Pr_2NiO_4-based mixed conductor. *J. Am. Chem. Soc.*, 2008, **130**, 2762-2763.

29.   X. Kuang, M. A. Green, H. Niu, P. Zajdel, C. Dickinson, J. B. Claridge, L. Jantsky and M. J. Rosseinsky, Interstitial oxide ion conductivity in the layered tetrahedral network melilite structure. *Nat. Mater.*, 2008, **7**, 498-504.

30.   M. Yashima *et al*. Direct evidence for two-dimensional oxide-ion diffusion in the hexagonal perovskite-related oxide $Ba_3MoNbO_{8.5−\delta}$. *J. Mater. Chem. A,* 2019, **7**, 13910-13916.

31.   S. Fop, E. J. Wildman, J. T. S. Irvine, P. A. Connor, J. M. S. Skakle, C. Ritter and A. C. Mclaughlin, Investigation of the relationship between the structure and conductivity of the novel oxide ionic conductor $Ba_3MoNbO_{8.5}$. *Chem. Mater.*, 2017, **29**, 4146-4152.

32.   K. S. McCombie, E. J. Wildman, C. Ritter, R. I. Smith, J. M. S. Skakle and A. C. Mclaughlin, The relationship between the crystal structure and electrical properties of the oxide ion conducting $Ba_3M'_{1+x}M''_{1-x}O_{8.5+x/2}$ (M' = W, Mo; M'' = Nb) phases, *Inorg. Chem.* 2018, **57**, 11942-11947.

33. D. Waroquiers, X. Gonze, G. M. Rignanese, C. Welker-Nieuwoudt, F. Rosowski, M. Göbel, S. Schenk, P. Degelmann, R. André, R. Glaum and G. Hautier, Statistical analysis of coordination environments in oxides. *Chem. Mater.*, 2017, **29**, 8346–8360.

34. D. N. Tawse, A. Gilane, S. Fop, A. Martinez-Felipe, F. Sher, R. I. Smith and A. C. Mclaughlin, An investigation of the crystal structure and ionic pathways of the hexagonal perovskite derivative $Ba_3VMoO_{8.5}$. *Inorg. Chem.*, 2021, **60**, 13550-13556.

35. S. Fop, K. S. McCombie, E. J. Wildman, J. M. S. Skakle, J. T. S. Irvine, P. A. Connor, C. Savaniu, C. Ritter and A. C. Mclaughlin, High oxide ion and proton conductivity in a disordered hexagonal perovskite, *Nat. Mater.*, **19**, 752-757 (2020).

36. S. Fop, J. A. Dawson, D. Fortes, C. Ritter and A. C. Mclaughlin, Hydration and ionic conduction mechanisms of hexagonal perovskite derivatives. *Chem. Mater.*, 2021, **33**, 4651-4660.

37. J. Cumby and J. P. Attfield, Ellipsoidal analysis of coordination polyhedra. *Nat. Commun.*, 2017, **8**, 1–8.

For table of contents only
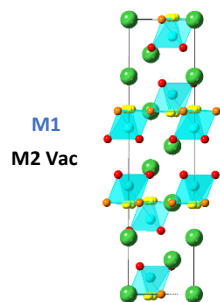
The presence of 50% V^{5+} on the M1 site in $Ba_3VWO_{8.5}$, which has a strong preference for tetrahedral geometry, is enough to disrupt the flexibility of the cation sublattice resulting in the ordering of the cations exclusively on the M1 site and no significant water absorption. This contrasts with other $Ba_3M'M''O_{8.5}$ phases which have cation disorder over the M1 and M2 sites and absorb significant amounts of water.

Supporting Information

for

A Variable Temperature Neutron Diffraction Study of the Oxide Ion Conductor Ba$_3$VWO$_{8.5}$

Asma Gilane [a, b], Sacha Fop [a, c], Dylan N. Tawse [a], Clemens Ritter [d] and Abbie C. Mclaughlin *[a]

[a] Department of Chemistry, University of Aberdeen, Meston Walk, Aberdeen AB24 3UE,

United Kingdom

[b] Lahore University of Management Sciences, Lahore, Pakistan.

[c] ISIS Facility, Rutherford Appleton Laboratory, Harwell Campus, Didcot, OX11 0QX, United Kingdom.

[d] Institut Laue Langevin, 71 Avenue des Martyrs, BP 156, F-38042 Grenoble Cedex 9, France.

*a.c.mclaughlin@abdn.ac.uk

Tel:0044 1224272924
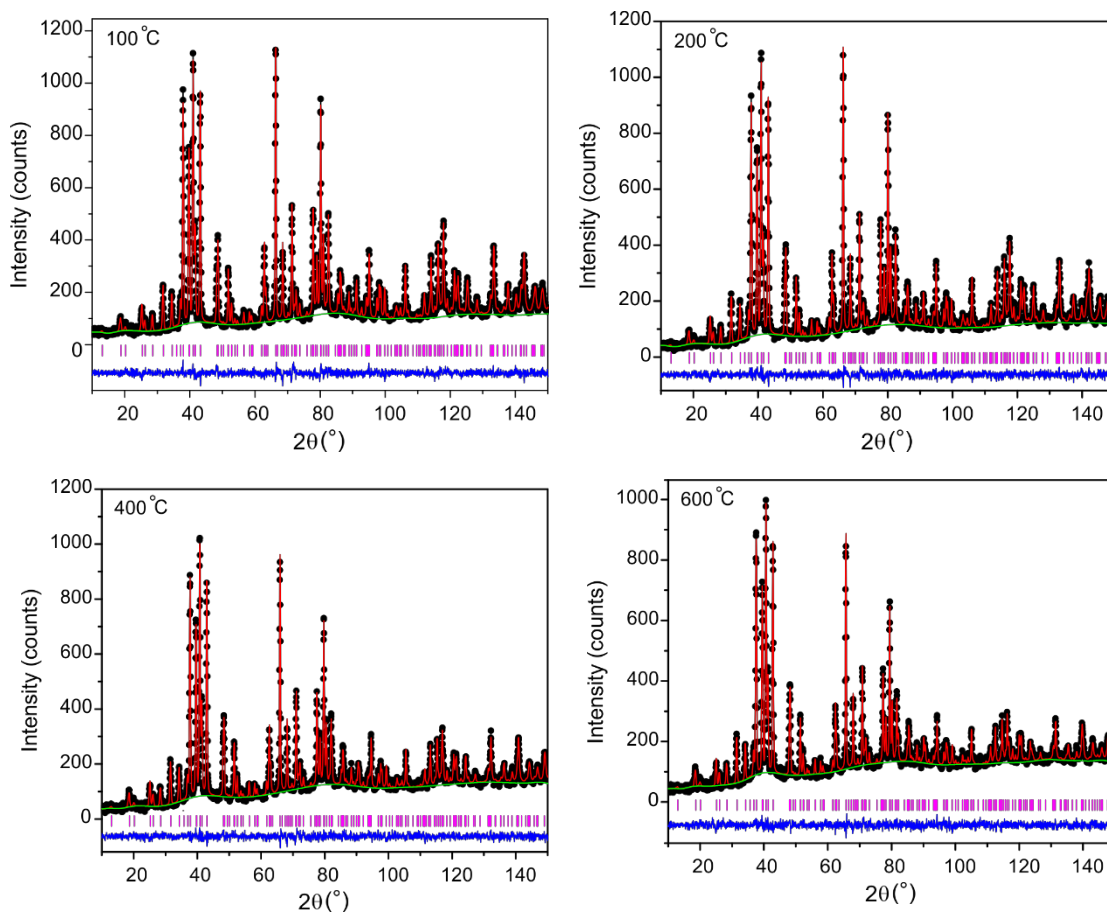
Figure S1 Rietveld fits to the $R\overline{3}m$ H crystallographic model of $Ba_3VWO_{8.5}$ at selected temperatures from neutron diffraction data. The black dots are the observed data and the red line is the Rietveld fit. The difference between the observed and the calculated patterns is shown by the blue line, the pink vertical bars indicate the reflection positions and the green line is the background function.
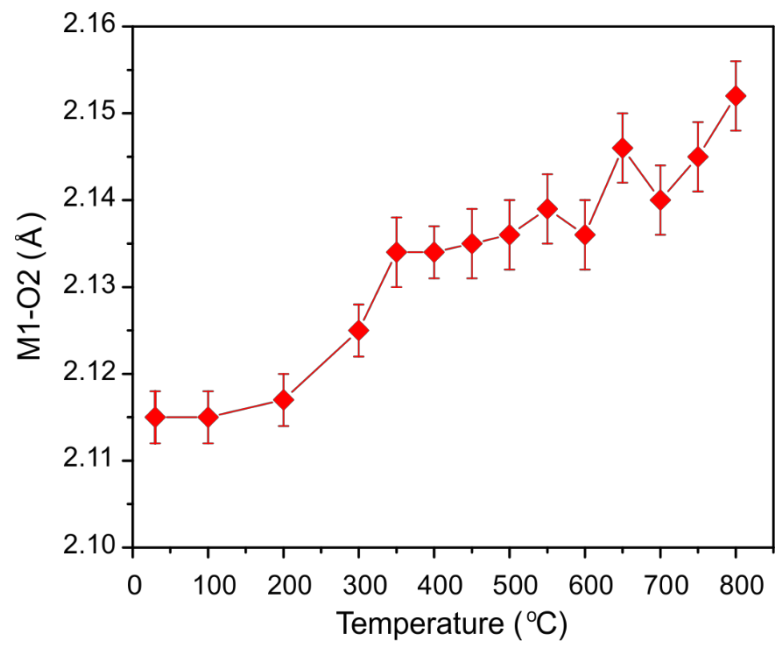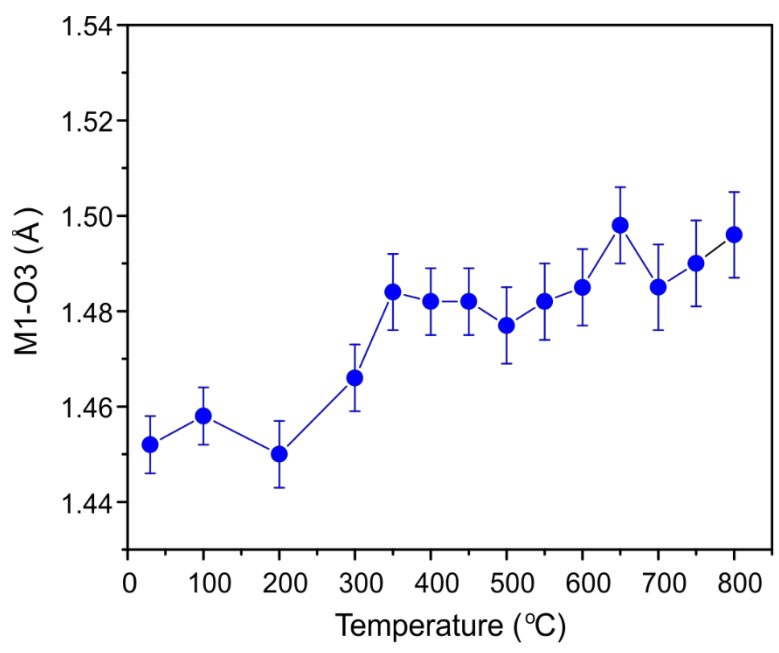
Figure S2. Temperature variation of the M1-O2 and M1-O3 bond lengths.
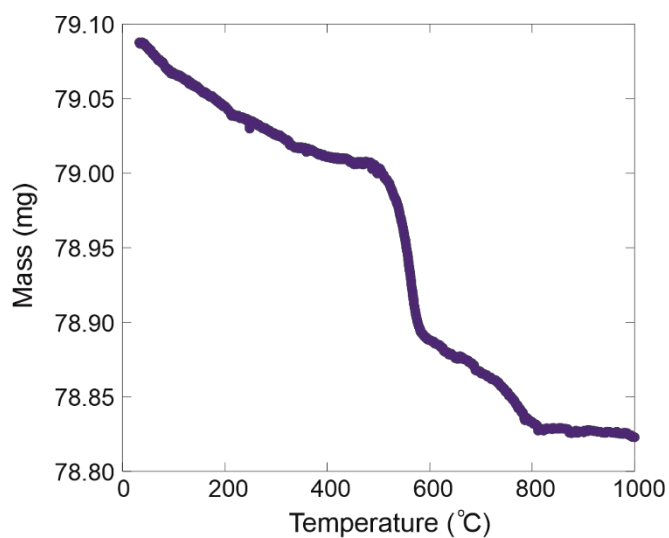
Figure S3. Thermogravimetric analysis performed in dry air on a sample of $Ba_3VWO_{8.5}$ stored under ambient conditions.
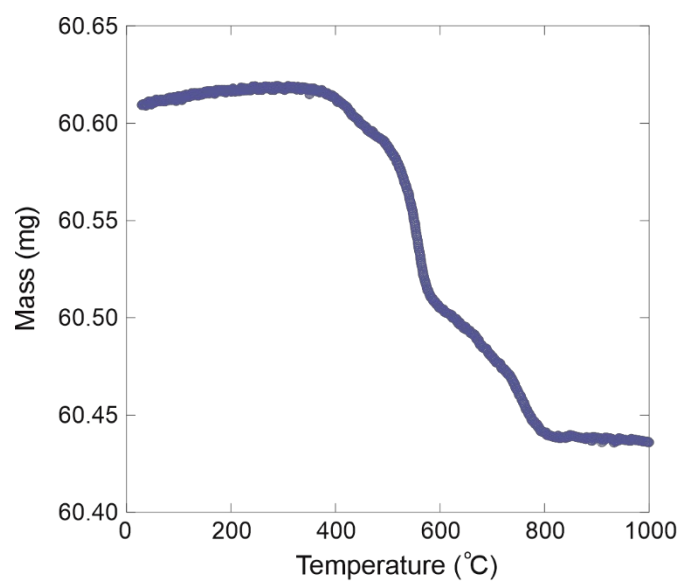
Figure S4. Thermogravimetric analysis performed in dry air on a sample of $Ba_3VWO_{8.5}$ after a two-hour pre-heat to remove the adsorbed species.
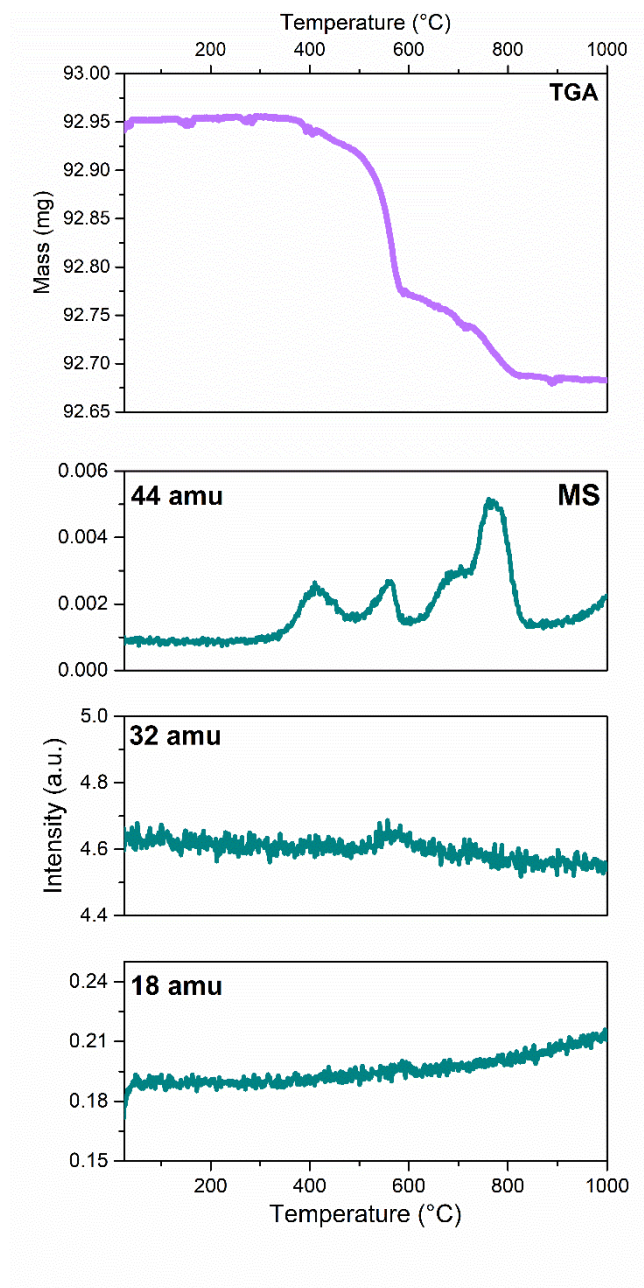
Figure S5 Results of the TGA-MS analysis on a $Ba_3VWO_{8.5}$ sample under dry air after a two-hour pre-heat to remove adsorbed species. The top panel shows the thermogravimetric (TGA) diagram, while the bottom ones are the mass spectroscopy diagrams obtained at 44 amu (CO_2), 32 amu (O_2) and 18 amu (H_2O).

Table S1 Crystallographic data table

Source	Neutron (constant wavelength)
Chemical formula	$Ba_3VWO_{8.5}$
Formula weight	782.7579
Temperature (K)	303
Crystal System	Trigonal
Space group	$R\bar{3}m$ H (no. 166)
a **(Å)**	5.8273(1)
c **(Å)**	21.1516(6)
V (Å³)	622.03(4)
Z	3
d-**space range (**Å)	0.8 – 13.2
χ^2	2.36
R_P	4.79
R_{WP}	5.76
Definition of R factors	$R_p = \Sigma|y_i(obs) - y_i(calc)|/\Sigma y_i(obs);$ $R_{wp} = \{\Sigma w_i[y_i(obs) - y_i(calc)]^2/\Sigma w_i y_i(obs)^2\}^{1/2}$

Table S2. Refined atomic parameters from Rietveld fit of the variable temperature neutron diffraction data of $Ba_3VWO_{8.5}$ recorded on the D2B diffractometer. Data were refined in the space group $R\bar{3}m$ H. Atom positions are Ba(1) (0, 0, 0), Ba(2) (0, 0, z), M(1) (0, 0, z), O(1) (x, y, z), O(2) (½, 0, 0), O(3) (x, y, z). U_{ij} indicates anisotropic thermal displacement parameters (in $Å^2$). U_{13} and U_{23} are zero due to the symmetry of the system. O(3) was refined with an isotropic thermal displacement parameter, U_{iso} (in $Å^2$).

Unit Cell			30 °C	100 °C	200 °C	300 °C	350 °C	400 °C	450 °C	500 °C	550 °C
a (Å)			5.8273 (1)	5.83320 (6)	5.84275 (7)	5.85332 (8)	5.85952 (9)	5.86526 (1)	5.87086 (8)	5.87613 (8)	5.88107 (8)
c (Å)			21.1516 (6)	21.1626 (4)	21.1818 (4)	21.2035 (3)	21.2171 (5)	21.2301 (5)	21.2419 (1)	21.2522 (5)	21.2605 (5)
V (Å³)			622.03 (4)	623.61 (2)	626.22 (2)	629.14 (2)	630.87 (2)	632.49 (2)	634.05 (2)	635.51 (2)	636.82 (2)
Atom	W	Parameter	30 °C	100 °C	200 °C	300 °C	350 °C	400 °C	450 °C	500 °C	550 °C
Ba(1)	3a	Occupancy	1	1	1	1	1	1	1	1	1
		$U_{11} = U_{22}$ (Å²)	0.0064 (7)	0.0131 (7)	0.0175 (8)	0.0201 (8)	0.0259 (9)	0.0273 (9)	0.0302 (9)	0.0301 (9)	0.0301 (9)
		U_{33} (Å²)	0.012 (1)	0.015 (1)	0.017 (1)	0.015 (1)	0.018 (1)	0.019 (1)	0.019 (1)	0.020 (1)	0.021 (1)
		U_{12} (Å²)	0.0032 (4)	0.0065 (4)	0.0087 (4)	0.010 (4)	0.0129 (4)	0.0136 (5)	0.0151 (5)	0.0150 (5)	0.0151 (5)
Ba(2)	6c	z	0.2064 (1)	0.2066 (1)	0.2067 (1)	0.2071 (1)	0.2069 (2)	0.2068 (1)	0.2068 (2)	0.2067 (2)	0.2068 (2)
		Occupancy	1	1	1	1	1	1	1	1	1
		$U_{11} = U_{22}$ (Å²)	0.0175 (7)	0.0151 (7)	0.0184 (8)	0.0209 (8)	0.0268 (9)	0.0282 (9)	0.0311 (9)	0.0309 (9)	0.0310 (9)
		U_{33} (Å²)	0.018 (1)	0.017 (1)	0.018 (1)	0.016 (1)	0.019 (1)	0.019 (1)	0.021 (1)	0.021 (1)	0.022 (1)
		U_{12} (Å²)	0.0087 (4)	0.0075 (4)	0.0092 (4)	0.0104 (4)	0.0134 (4)	0.0141 (5)	0.0155 (5)	0.0154 (5)	0.0155 (5)
M(1)	6c	z	0.3939 (2)	0.3937 (2)	0.3937 (2)	0.3941 (2)	0.3947 (3)	0.3945 (3)	0.3944 (3)	0.3944 (3)	0.3945 (3)
		Occupancy	1	1	1	1	1	1	1	1	1
		$U_{11} = U_{22}$ (Å²)	0.0077 (3)	0.012 (1)	0.013 (2)	0.013 (2)	0.021 (2)	0.015 (2)	0.018 (2)	0.020 (2)	0.023 (2)
		U_{33} (Å²)	0.012 (2)	0.008 (2)	0.014 (3)	0.016 (3)	0.029 (3)	0.017 (3)	0.021 (3)	0.021 (3)	0.017 (3)
		U_{12} (Å²)	0.0038 (7)	0.0051 (7)	0.0069 (8)	0.0068 (8)	0.0109 (9)	0.0076 (8)	0.0091 (9)	0.0101 (9)	0.0119 (9)

O(1)	18*h*	*x*	0.1731 (1)	0.1729 (1)	0.1731 (2)	0.1734 (2)	0.1732 (2)	0.1738 (2)	0.1737 (2)	0.1739 (2)	0.1738 (2)
		y	0.8269 (1)	0.8271 (1)	0.8268 (2)	0.8265 (2)	0.8267 (2)	0.8261 (2)	0.8262 (2)	0.8261 (2)	0.8261 (2)
		z	0.10210 (6)	0.10188 (6)	0.10183 (6)	0.10165 (6)	0.10161 (7)	0.10148 (6)	0.1014 (6)	0.10146 (7)	0.10145 (7)
		Occupancy	1	1	1	1	1	1	1	1	1
		$U_{11} = U_{22}$ (Å^2)	0.0138 (6)	0.0172 (6)	0.0213 (7)	0.0241 (7)	0.0286 (7)	0.0296 (8)	0.0314 (8)	0.0327 (9)	0.0355 (8)
		U_{33} (Å^2)	0.0162 (9)	0.0147 (8)	0.0185 (9)	0.0232 (9)	0.0271 (9)	0.0281 (9)	0.0282 (9)	0.029 (1)	0.031 (1)
		U_{12} (Å^2)	0.0116 (6)	0.0137 (7)	0.0161 (7)	0.0192 (8)	0.0219 (8)	0.0229 (9)	0.0242 (9)	0.0255 (9)	0.0277 (9)
O(2)	9*e*	Occupancy	0.370 (3)	0.368 (3)	0.361 (3)	0.359 (3)	0.353 (4)	0.353 (4)	0.353 (4)	0.353 (4)	0.354 (4)
		$U_{11} = U_{22}$ (Å^2)	0.052 (2)	0.049 (2)	0.049 (2)	0.0583 (7)	0.059 (3)	0.061 (3)	0.064 (3)	0.067 (3)	0.077 (3)
		U_{33} (Å^2)	0.026 (3)	0.030 (3)	0.031 (4)	0.030 (4)	0.027 (4)	0.030 (4)	0.034 (4)	0.031 (4)	0.025 (4)
		U_{12} (Å^2)	0.026 (1)	0.025 (9)	0.024 (1)	0.0291 (4)	0.029 (1)	0.031 (1)	0.032 (1)	0.033 (2)	0.038 (2)
O(3)	36*i*	*x*	0.055 (1)	0.057 (1)	0.055 (2)	0.061 (1)	0.062 (1)	0.060 (2)	0.061 (2)	0.058 (2)	0.061 (2)
		y	0.035 (6)	0.046(2)	0.009 (3)	0.011 (3)	0.011 (3)	0.005 (2)	0.003 (2)	0.001 (3)	0.002 (3)
		z	0.3266 (2)	0.3264 (2)	0.3267 (2)	0.3267 (2)	0.3264 (2)	0.3265 (2)	0.3266 (2)	0.3267 (2)	0.3268 (2)
		Occupancy	0.116 (1)	0.116 (1)	0.118 (1)	0.118 (1)	0.120 (1)	0.120 (1)	0.120 (1)	0.120 (1)	0.120 (1)
		U_{iso} (Å^2)	0.020 (2)	0.017 (2)	0.025 (2)	0.024 (2)	0.026 (3)	0.028 (3)	0.030 (3)	0.036 (3)	0.036 (3)
χ^2			2.36	2.27	2.20	2.21	2.24	1.98	2.06	1.99	1.95
R_p (%)			4.79	4.80	4.94	4.91	4.99	4.71	4.74	4.6	4.57
R_{wp} (%)			5.76	5.76	5.82	5.87	5.95	5.59	5.72	5.54	5.50

Unit Cell			600 °C	650 °C	700 °C	750 °C	800 °C
a (Å)			5.88650 (9)	5.89214 (9)	5.8979 (1)	5.9036 (1)	5.9093 (1)
c (Å)			21.2708 (5)	21.2821 (5)	21.2954 (6)	21.3077 (6)	21.3211 (6)
V (Å³)			638.31 (3)	639.86 (3)	641.52 (3)	643.14 (3)	644.78 (3)
Atom	W	Parameter	600 °C	650 °C	700 °C	750 °C	800 °C
Ba(1)	3a	Occupancy	1	1	1	1	1
		$U_{11} = U_{22}$ (Å²)	0.029 (1)	0.032 (1)	0.033 (1)	0.035 (1)	0.036 (1)
		U_{33} (Å²)	0.024 (2)	0.024 (2)	0.027 (2)	0.027 (2)	0.027 (2)
		U_{12} (Å²)	0.0149 (5)	0.0163 (6)	0.0169 (6)	0.0177 (6)	0.0181 (6)
Ba(2)	6c	z	0.2067 (2)	0.2068 (2)	0.2069 (2)	0.2073 (2)	0.2072 (2)
		Occupancy	1	1	1	1	1
		$U_{11} = U_{22}$ (Å²)	0.031 (1)	0.033 (1)	0.034 (1)	0.036 (1)	0.037 (1)
		U_{33} (Å²)	0.025 (1)	0.025 (2)	0.027 (2)	0.028 (2)	0.028 (2)
		U_{12} (Å²)	0.0154 (5)	0.0168 (6)	0.0173 (6)	0.0182 (6)	0.0185 (6)
M(1)	6c	z	0.3942 (3)	0.3948 (3)	0.3943 (3)	0.3945 (3)	0.3948 (3)
		Occupancy	1	1	1	1	1
		$U_{11} = U_{22}$ (Å²)	0.022 (2)	0.021 (2)	0.023 (2)	0.023 (2)	0.021 (2)
		U_{33} (Å²)	0.024 (3)	0.022 (3)	0.024 (4)	0.021 (4)	0.027 (4)
		U_{12} (Å²)	0.011 (1)	0.011 (1)	0.011 (1)	0.011 (1)	0.011 (1)
O(1)	18h	x	0.1743 (2)	0.1743 (2)	0.1743 (2)	0.1746 (2)	0.1748 (2)
		y	0.8256 (2)	0.8256 (2)	0.8256 (2)	0.8253 (2)	0.8251 (2)
		z	0.10158 (7)	0.10138 (7)	0.10133 (8)	0.10113 (8)	0.10111 (8)
		Occupancy	1	1	1	1	1

		$U_{11} = U_{22}$ (Å^2)	0.0361 (9)	0.0390 (9)	0.0411 (9)	0.042 (1)	0.045 (1)
		U_{33} (Å^2)	0.031 (1)	0.034 (1)	0.034 (1)	0.037 (1)	0.039 (1)
		U_{12} (Å^2)	0.028 (1)	0.031 (1)	0.032 (1)	0.033 (1)	0.034 (1)
O(2)	9e	Occupancy	0.350 (5)	0.351 (5)	0.353 (5)	0.350 (5)	0.349 (5)
		$U_{11} = U_{22}$ (Å^2)	0.072 (3)	0.077 (4)	0.082 (4)	0.081 (4)	0.084 (4)
		U_{33} (Å^2)	0.030 (5)	0.028 (5)	0.028 (5)	0.028 (5)	0.035 (5)
		U_{12} (Å^2)	0.036 (2)	0.038 (2)	0.041 (2)	0.040 (2)	0.042 (2)
O(3)	36i	x	0.064 (2)	0.062 (2)	0.067 (2)	0.067 (2)	0.064 (2)
		y	0.005 (3)	0.001 (3)	0.004 (3)	0.004 (3)	0.001 (3)
		z	0.3265 (3)	0.3266 (2)	0.3268 (3)	0.3269 (3)	0.3271 (3)
		Occupancy	0.121 (1)	0.120 (1)	0.120 (1)	0.121 (1)	0.122 (2)
		U_{iso} (Å^2)	0.039 (3)	0.035 (3)	0.036 (3)	0.038 (3)	0.041 (4)
χ^2			1.98	1.95	2.06	2.09	1.91
R_p (%)			4.57	4.49	4.61	4.67	4.45
R_{wp} (%)			5.49	5.44	5.61	5.66	5.43

Table S3. Refined bond length and angle values obtained from Rietveld fits of the variable-temperature neutron data for Ba₃VWO₈.₅.

Distance (Å)	30 °C	100 °C	200 °C	300 °C	350 °C	400 °C	450 °C	500 °C	550 °C
Ba(1)–O(1)	2.778 (1)	2.775 (1)	2.779 (1)	2.782 (2)	2.782 (2)	2.786 (2)	2.786 (2)	2.790 (2)	2.791 (2)
Ba(1)–O(2)	2.91364 (7)	2.91658 (3)	2.92138 (3)	2.92666 (4)	2.92976 (4)	2.93263 (4)	2.93543 (4)	2.93807 (4)	2.94054 (4)
Ba(1)–O(3)	3.090 (7)	3.083 (7)	3.097 (8)	3.077 (7)	3.074 (7)	3.087 (8)	3.088 (9)	3.104 (11)	3.091 (9)
Ba(2)–O(1)	2.815 (3)	2.822 (3)	2.829 (3)	2.845 (3)	2.843 (3)	2.850 (3)	2.853 (3)	2.853 (3)	2.857 (3)
	2.9610 (5)	2.9644 (5)	2.9689 (5)	2.9734 (5)	2.9773 (6)	2.9811 (5)	2.9844 (6)	2.9870 (6)	2.9891 (6)
Ba(2)–O(2)	3.167 (2)	3.167 (3)	3.168 (3)	3.165 (3)	3.171 (3)	3.174 (3)	3.177 (3)	3.180 (3)	3.180 (3)
Ba(2)–O(3)	2.555 (4)	2.554 (4)	2.561 (4)	2.557 (4)	2.558 (6)	2.563 (5)	2.569 (5)	2.573 (5)	2.574 (5)
M(1)–O(1)	1.841 (3)	1.84 (3)	1.844 (3)	1.838 (3)	1.835 (3)	1.832 (3)	1.834 (3)	1.835 (3)	1.836 (3)
M(1)–O(2)	2.114 (3)	2.115 (3)	2.117 (3)	2.125 (3)	2.136 (4)	2.134 (3)	2.135 (4)	2.136 (4)	2.139 (4)
M(1)–O(3)	1.451 (6)	1.459 (6)	1.450 (7)	1.466 (7)	1.489 (7)	1.482 (7)	1.482 (7)	1.477 (8)	1.482 (8)
O(1)–M(1)–O(1)	99.1 (2)	99.2 (2)	99.2 (2)	99.6 (2)	100.2 (2)	100.0 (2)	100.0 (2)	99.9 (2)	100.0 (2)
O(1)–M(1)–O(2)	86.54 (4)	86.43 (4)	86.40 (4)	86.29 (5)	86.14 (5)	86.18 (5)	86.13 (5)	86.17 (5)	86.13 (5)
	171.3 (2)	171.2 (2)	171.2 (3)	170.8 (3)	170.0 (3)	170.3 (3)	170.3 (3)	170.4 (3)	170.3 (3)
O(1)–M(1)–O(3)	107.5 (3)	106.9 (3)	107.2 (3)	105.9 (3)	105.8 (3)	105.4 (3)	105.6 (3)	106.1 (4)	105.5 (4)
	122.1 (14)	119.5 (5)	119.7 (6)	119.4 (6)	119.0 (6)	118.2 (5)	117.6 (5)	117.4 (6)	117.4 (5)
	125.1 (13)	127.4 (5)	127.4 (6)	127.8 (5)	127.4 (5)	128.3 (4)	128.9 (4)	128.9 (5)	129.2 (5)
O(2)–M(1)–O(2)	87.1 (2)	87.2 (1)	87.3 (2)	87.0 (2)	86.6 (2)	86.8 (2)	86.9 (2)	86.9 (2)	86.8 (2)

Distance (Å)	600 °C	650 °C	700 °C	750 °C	800 °C
Ba(1)–O(1)	2.798 (2)	2.797 (2)	2.798 (2)	2.799 (2)	2.802 (2)
Ba(1)–O(2)	2.94325 (5)	2.94607 (5)	2.94895 (5)	2.95182 (5)	2.95466 (5)
Ba(1)–O(3)	3.075 (9)	3.089 (10)	3.066 (9)	3.070 (9)	3.090 (11)
Ba(2)–O(1)	2.856 (3)	2.864 (3)	2.866 (4)	2.883 (4)	2.883 (4)
	2.9921 (6)	2.9953 (6)	2.9980 (7)	3.0000 (7)	3.0032 (7)
Ba(2)–O(2)	3.185 (3)	3.185 (3)	3.185 (3)	3.180 (3)	3.183 (3)
Ba(2)–O(3)	2.576 (5)	2.577 (5)	2.584 (6)	2.578 (6)	2.584 (6)
M(1)–O(1)	1.838 (4)	1.831 (3)	1.837 (4)	1.832 (4)	1.829 (4)
M(1)–O(2)	2.136 (4)	2.146 (4)	2.142 (4)	2.146 (4)	2.152 (4)
M(1)–O(3)	1.485 (8)	1.498 (8)	1.489 (9)	1.491 (9)	1.496 (9)
O(1)–M(1)–O(1)	99.6 (2)	100.2 (2)	100.0 (3)	100.2 (3)	100.4 (3)
O(1)–M(1)–O(2)	86.26 (6)	86.08 (6)	86.10 (6)	86.02 (6)	85.96 (6)
	170.8 (3)	170.0 (3)	170.5 (3)	170.2 (4)	169.9 (4)
O(1)–M(1)–O(3)	105.0 (4)	105.0 (4)	104.2 (4)	104.0 (4)	104.4 (4)
	118.2 (6)	116.8 (5)	117.7 (6)	117.5 (6)	116.2 (6)
	129.6 (5)	129.6 (4)	130.0 (5)	129.9 (5)	130.2 (5)
O(2)–M(1)–O(2)	87.1 (2)	86.7 (2)	87.0 (2)	86.9 (2)	86.7 (2)